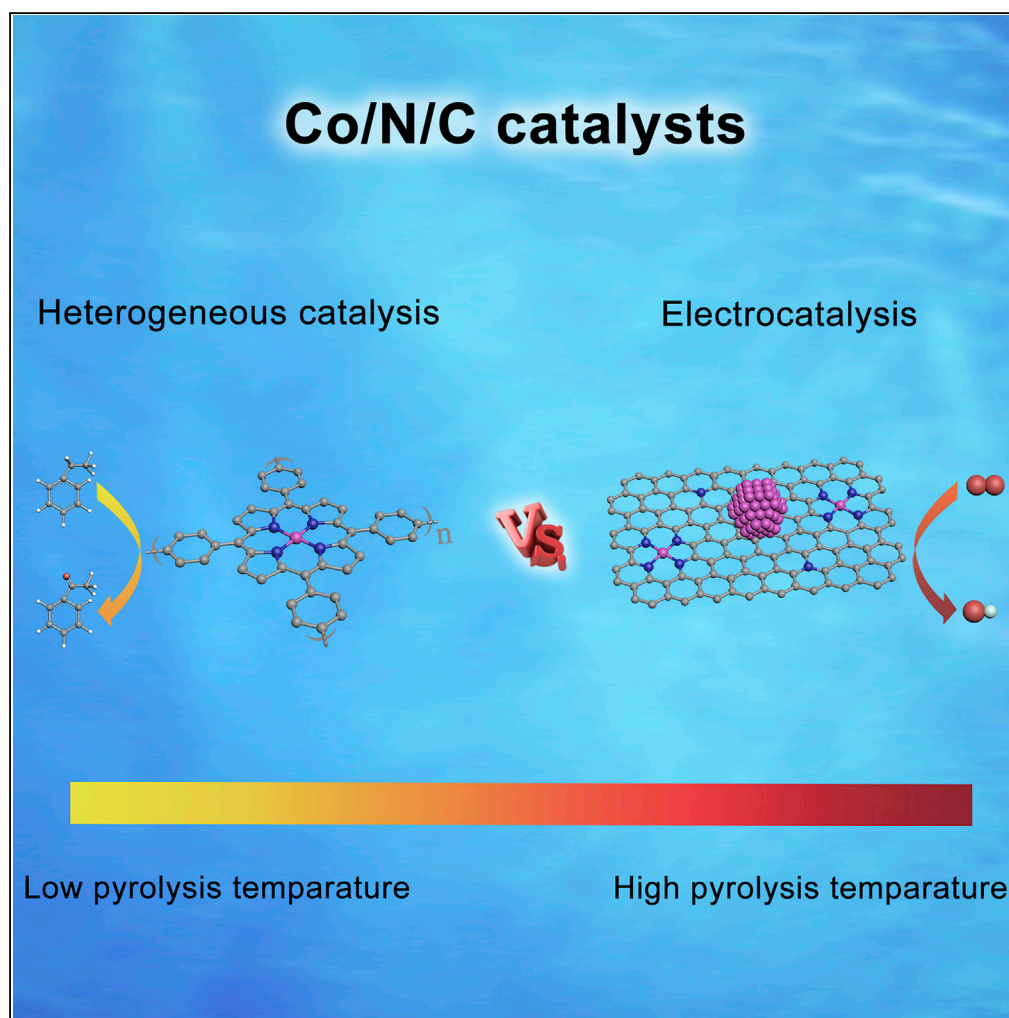**Article**

Switching Co/N/C Catalysts for Heterogeneous Catalysis and Electrocatalysis by Controllable Pyrolysis of Cobalt Porphyrin

Zhen-Yu Wu, Ming-Xi Chen, Sheng-Qi Chu, Yue Lin, Hai-Wei Liang, Jing Zhang, Shu-Hong Yu

hwliang@ustc.edu.cn (H.-W.L.)
shyu@ustc.edu.cn (S.-H.Y.)

HIGHLIGHTS

A group of mesoporous Co/N/C catalysts have been successfully prepared

HAADF-STEM and XAFS reveal structural and componential information of the catalysts

The difference in optimizing Co/N/C catalysts for different reactions is identified

Article

Switching Co/N/C Catalysts for Heterogeneous Catalysis and Electrocatalysis by Controllable Pyrolysis of Cobalt Porphyrin

Zhen-Yu Wu,[1,3] Ming-Xi Chen,[1,3] Sheng-Qi Chu,[2] Yue Lin,[1] Hai-Wei Liang,[1,*] Jing Zhang,[2] and Shu-Hong Yu[1,4,*]

SUMMARY

Identifying the optimal synthetic and structural parameters in preparing pyrolyzed metal/nitrogen/carbon (M/N/C) materials is crucial for developing effective catalysts for many important catalytic processes. Here we report a group of mesoporous Co/N/C catalysts ranging from polymerized cobalt porphyrin to Co/N-doped carbons, which are prepared by pyrolysis of cobalt porphyrin using silica nanoparticles as templates at different temperatures, for boosting both heterogeneous catalysis and electrocatalysis. It is revealed that the polymerized cobalt porphyrin prepared at low temperature (500°C) is a polymer-like network with exclusive single-atom Co-N_x sites, and that the high-temperature-pyrolysis (>600°C) produces an electrically conductive Co/N-doped carbon, accompanied by part degradation of Co-N_x centers. We identify that the polymerized cobalt porphyrin with undecomposed Co-N_x centers is optimal for heterogeneous catalytic oxidation of ethylbenzene, whereas the electrically conductive Co/N-doped carbon is ideal for eletrocatalytic oxygen reduction. Our results provide new insights for rationally optimizing M/N/C catalysts for different reactions.

INTRODUCTION

Catalysis, which can accelerate the speed of chemical reactions by changing the reaction pathway and lowering the activation energy, plays a crucial role in diverse fields, such as electrochemical energy conversion (Seh et al., 2017; Jiao et al., 2015; Liu et al., 2018; Bayatsarmadi et al., 2017; Meng et al., 2017), petrochemical industry (Marcilly, 2003), organic synthesis chemistry (Bauer and Knölker. 2015; Suzuki, 2011; Lyons and Sanford. 2010), and living systems (Neitzel, 2010). Particularly, electrocatalysis for energy conversion and heterogeneous catalysis for molecule transformation have received extensive attention, owing to their great application potential and high fundamental research value (Seh et al., 2017; Jiao et al., 2015; Bauer and Knölker. 2015; Suzuki, 2011). Currently, the most effective catalysts for these reactions are generally precious metals and their alloys or complexes (Jiao et al., 2015; Suzuki, 2011; Lyons and Sanford. 2010). However, the prohibitive cost and scarcity of precious metals hinder their widespread technological use and therefore have spurred many interests in developing non-precious metal catalysts (NPMCs) with earth-abundant elements for these catalytic processes (Jiao et al., 2015; He et al., 2016).

Pyrolyzed metal/nitrogen/carbon (M/N/C, M = Fe, Co, Ni, etc.) compounds, typical NPMCs, exhibit excellent catalytic performance for various electrochemical processes, particularly for the oxygen reduction reaction (ORR) (Bezerra et al., 2008; Chen et al., 2011; Jaouen et al., 2011; Lefèvre et al., 2009; Wu et al., 2011a; Wang et al., 2017; Chung et al., 2017). It is found that the electrocatalytic performance of M/N/C catalysts is strongly dependent on the intrinsic nature of M-N_x active sites, numbers of exposed active sites, porous structure, and electrical conductivity (Jaouen et al., 2011; Liang et al., 2013; Wu et al., 2015). Based on these in-depth understanding, now the rationally prepared M/N/C catalysts can compete with platinum-based catalysts in acidic medium and even surpass platinum-based counterparts in alkaline medium for ORR (Wang et al., 2017; Chung et al., 2017; Liang et al., 2013; Yin et al., 2016). The great success of M/N/C catalysts in eletrocatalysis encourages considerable research works in employing these NPMCs for heterogeneous catalysis in various organic reactions (He et al., 2016; Jagadeesh et al., 2017; Liu et al., 2016a, 2016b, 2017; Zhou et al., 2017), including selective oxidation (Jagadeesh et al., 2013a), selective hydrogenation (Jagadeesh et al., 2013b), epoxidation (Banerjee et al., 2014), oxidative dehydrogenation (Cui et al., 2015), reductive amination (Jagadeesh et al., 2017), hydrogenative coupling of nitroarenes, and C-C coupling reactions (Liu et al., 2016a; Zhang et al., 2015). In spite of these progresses, the understanding of structure-performance relationship of M/N/C catalysts for heterogeneous catalysis is very limited,

[1]Division of Nanomaterials & Chemistry, Hefei National Laboratory for Physical Sciences at the Microscale, CAS Center for Excellence in Nanoscience, Hefei Science Center of CAS, Collaborative Innovation Center of Suzhou Nano Science and Technology, Department of Chemistry, University of Science and Technology of China, Hefei 230026, China

[2]Institute of High Energy Physics, Chinese Academy of Sciences, Beijing 100049, China

[3]These authors contributed equally

[4]Lead Contact

*Correspondence:
hwliang@ustc.edu.cn
(H.-W.L.),
shyu@ustc.edu.cn (S.-H.Y.)
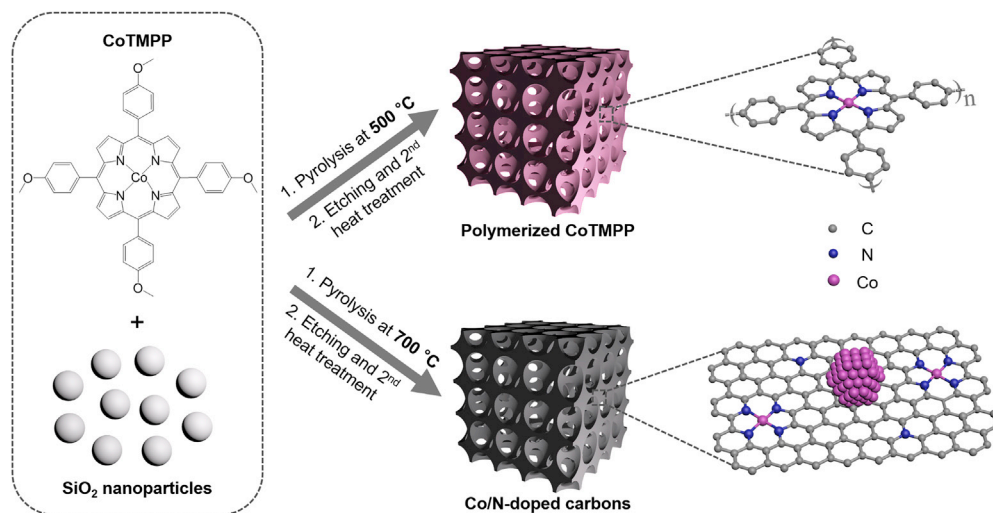https://doi.org/10.1016/j.isci.2019.04.032

Figure 1. Catalyst Preparation

Schematic illustration of the preparation of mesoporous polymerized CoTMPP and Co/N-doped carbons from CoTMPP and SiO_2 templates.

compared with that for electrocatalysis. The identification of the difference in designing and optimizing M/N/C materials for electrocatalysis and heterogeneous catalysis is therefore urgently necessary for developing high-performance M/N/C catalysts for various organic reactions.

Generally, to boost electrocatalysis, high pyrolysis temperature is needed to endow the M/N/C materials with high electrical conductivity for efficient electron transport from the active centers within the catalysts to the electrode (Bezerra et al., 2008; Jaouen et al., 2011). Nevertheless, such long-range electron transport is absent in the heterogeneous catalysis for organic reactions (He et al., 2016). This seems to suggest that the optimal M/N/C materials for heterogeneous catalysis should be prepared at a lower temperature than that for electrocatalysis, as high-temperature pyrolysis would inevitably destroy the highly active single-atom M-N_x active sites to form less-active metallic nanoparticles. To identify the difference in optimizing the M/N/C catalysts for electrocatalysis and heterogeneous catalysis, herein we develop a group of mesoporous Co/N/C materials, ranging from polymerized cobalt porphyrin to Co/N-doped carbons, which are prepared by the pyrolysis of cobalt porphyrin with silica nanoparticle templates under different temperatures and studied for both heterogeneous catalysis in organic reactions and electrocatalysis in a comparative perspective.

RESULTS

Catalyst Preparation

The Co/N/C catalysts were prepared by pyrolysis of cobalt tetramethoxyphenylporphyrin (CoTMPP, a typical Co porphyrin molecule) under N_2 at 400°C–800°C with SiO_2 nanoparticles (fumed powder, 7 nm) as hard templates, before NaOH etching to remove the templates and the second heat treatment (Figure 1). The obtained catalysts are denoted as CoTMPP-x, where x is the pyrolysis temperature. To understand the pyrolysis behavior of the CoTMPP precursor, thermogravimetric analysis (TGA) tests were first conducted for CoTMPP/SiO_2 mixture as well as for individual CoTMPP and SiO_2. The differential thermogravimetric (DTG) curve of CoTMPP/SiO_2 mixture matches well with those of pure CoTMPP and SiO_2, indicating a similar thermal decomposition process for CoTMPP with or without SiO_2 templates (Figures 2A and S1). The first weight loss of 1.08% before 255°C for pure CoTMPP is attributed to the loss of the physically absorbed water and residual small organic molecules for synthesizing CoTMPP (Figure 2A). The subsequent weight loss of 9.36% from 225°C to 485°C is ascribed to the demethylation and demethoxylation reactions of CoTMPP. Therefore the thermal polymerization of the CoTMPP unit is completed during this step, which is consistent with previous reports on the thermal polymerization behavior of Co porphyrin and Co phthalocyanine (Zhou et al., 2017; Ji et al., 2011). The third weight loss step (16.59%) is observed from 485°C to 800°C, which is due to the further decomposition of polymeric intermediates and the formation of
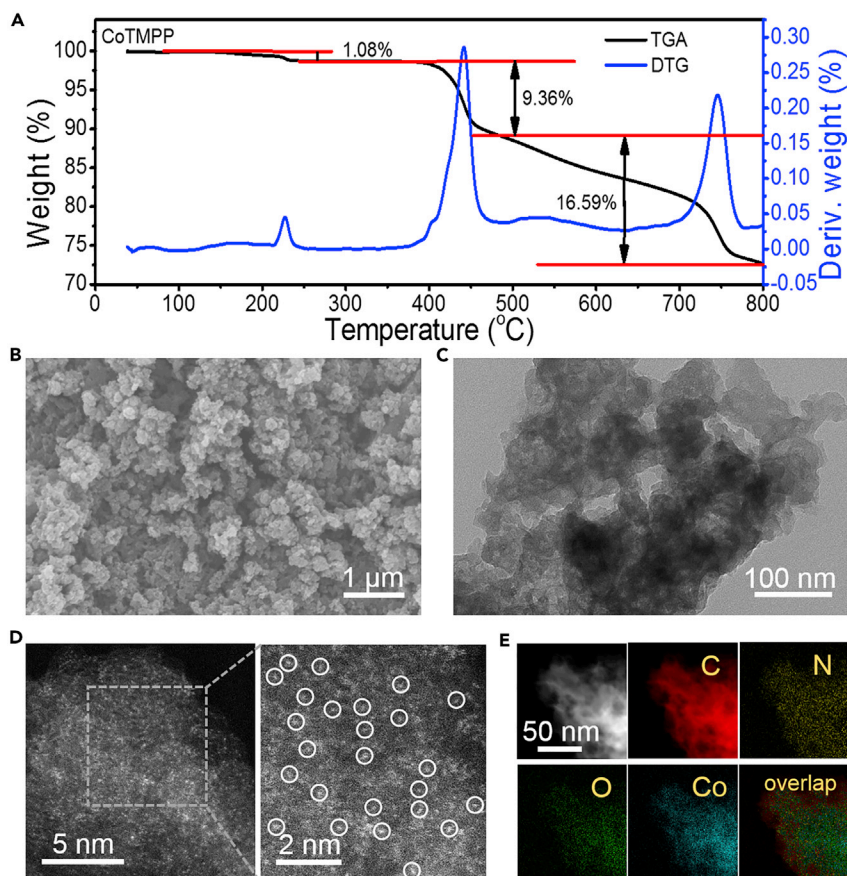
Figure 2. Catalyst Characterization

(A) TGA and differential thermogravimetry curves of pure CoTMPP molecule.

(B–E) (B) SEM, (C) TEM, (D) aberration-corrected HAADF-STEM, and (E) electron energy-loss spectroscopic elemental mapping images of the CoTMPP-500 catalyst.

graphitic materials. At this stage, the Co-N$_4$ centers originated from CoTMPP are partially or completely decomposed to form metallic Co nanoparticles.

Catalyst Characterization

Solid ultraviolet-visible (UV-vis) spectra were used to investigate the structural changes of CoTMPP after thermal treatment (Figure S2). The peaks at 535 and 579 nm (Q band) become weak in CoTMPP-400, 500 compared with the CoTMPP molecule, whereas the peak at 637 nm (Q band) in CoTMPP molecule shifts to 622 nm in CoTMPP-400, 500, revealing the part damage of Co porphyrin molecular structure at the heat treatment temperature of 400°C–500°C. With further increase in the treatment temperature, no obvious peak is observed for CoTMPP-600, 700, indicating that most of the Co porphyrin structure is destroyed. Elemental analysis (EA) and X-ray photoelectron spectroscopy (XPS) were performed to probe the chemical compositions and element bonding configurations of CoTMPP-x catalysts. As revealed by the EA tests, the N/C weight ratios of CoTMPP-400 (0.0967) and CoTMPP-500 (0.10) are almost the same as that of CoTMPP molecule (0.0972), suggesting that the main molecular structure of CoTMPP is retained after pyrolysis at temperature below 500°C. With the increase of the pyrolysis temperature to 600°C and 700°C, however, the N/C weight ratio decreases considerably to 0.090 and 0.063, respectively, indicating the decomposition of Co-N$_4$ centers in CoTMPP molecules. The XPS survey spectrum displays the presence of C, N, O, and Co in all the CoTMPP-x catalysts (Figure S3A). With the increase of the pyrolysis temperature, the surface C contents increase, whereas the surface O contents decrease accordingly (Table S1). High-resolution N 1s XPS spectrum of CoTMPP molecule shows only one peak at 399.0 eV, corresponding to pyrrolic N (Figure S3B). After heat treatment, a new peak at around 400.6 eV that corresponds to

graphic N emerges for the CoTMPP-*x* catalysts (Figures S3C–S3F) (Wu et al., 2015; Yang et al., 2011). The graphitic N takes up 17.1%, 28.6%, 45.4%, and 52.4% N contents of CoTMPP-400, 500, 600, and 700, respectively, further confirming that higher pyrolysis temperature leads to more serious destruction of CoTMPP molecule units.

The microstructures of the CoTMPP-*x* catalysts were examined by scanning electron microscopy (SEM) and transmission electron microscopy (TEM) (Figures 2B, 2C, and S4). Interconnected porous structure is observed for all SiO$_2$-templated catalysts except CoTMPP-400; probably the pyrolysis at 400°C cannot generate mechanically robust polymer/carbon structure on SiO$_2$ templates (see TGA results). In addition, no nanoparticles are observed anywhere in the cases of CoTMPP-400, 500, whereas a large number of nanoparticles appear in the catalysts when the pyrolysis temperature is higher than 600°C. Aberration-corrected high-angle annular dark-field scanning transmission electron microscopic (HAADF-STEM) images of CoTMPP-500 reveal that the brighter spots assigned to the Co atoms dominantly present the atomic dispersion (Figure 2D). The isolated heavier Co single atoms can be discerned in the polymer-like structure because of the different Z contrasts of Co, N, C, and O elements (Yin et al., 2016). Careful examinations of different areas confirm the absence of Co clusters or nanoparticles in CoTMPP-500 (Figure S5). The electron energy-loss spectroscopy elemental mapping images show that Co, N, C, and O are distributed uniformly over the entire architecture of CoTMPP-500 (Figure 2E). For CoTMPP-700, the HAADF-STEM images show the presence of numerous isolated Co single atoms as well (Figures S6A and S6B), although accompanied with highly crystalline Co nanoparticles (Figures S6C and S6D). In addition, elemental mapping also confirms the coexistence of Co single-atom sites and nanoparticles in CoTMPP-700 (Figure S7). X-ray diffraction analyses further affirm the formation of metallic cobalt phase in CoTMPP-700 and CoTMPP-800, whereas CoTMPP-500 is free of any crystalline inorganic phase (Figure S8).

The porous structures of the CoTMPP-*x* catalysts were further investigated by N$_2$ adsorption/desorption measurement (Figures S9 and S10). Except for CoTMPP-400, the isotherms of all CoTMPP-*x* samples show typical type IV curves with a distinct hysteresis loop in the range of 0.4–1.0 P/P$_0$, indicating the mesoporous nature of these catalysts. As expected, the non-porous CoTMPP-400 catalyst exhibits a low Brunauer-Emmett-Teller (BET) surface area and pore volume of only 8.8 m^2 g^{-1} and 0.016 cm^3 g^{-1}, respectively. Importantly, the BET surface area greatly increases to 380 m^2 g^{-1} for CoTMPP-500 and further slightly increases to 486 m^2 g^{-1} for CoTMPP-800 because of the formation of robust mesoporous polymer/carbon structures. The pore volume of CoTMPP-*x* also gradually increases from 0.82 to 1.29 cm^3 g^{-1} when the pyrolysis temperature increases from 500°C to 800°C. Note that the reference sample prepared without SiO$_2$ templates (CoTMPP-500/SiO$_2$-free) exhibits much lower BET surface area (4.95 m^2 g^{-1}) and pore volume (0.0055 cm^3 g^{-1}) than CoTMPP-500.

To investigate the local atomic and coordination structures of the CoTMPP-*x* catalysts, X-ray absorption near-edge structure (XANES) and extended X-ray absorption fine structure (EXAFS) were carried out. The CoTMPP molecule features a pre-edge peak at 7,714 eV, which is regarded as the fingerprint of square planar Co-N$_4$ moieties (Figures 3A and S11) (Liu et al., 2016a). The absorption threshold and white line peak intensity in the Co K-edge XANES curves of CoTMPP-*x* catalysts are between those of CoTMPP molecule and Co foil (Figure 3A), indicating that the valence states of Co element in the CoTMPP-*x* samples are situated between those of Co^0 and Co^{II} (Yin et al., 2016). Notably, the absorption thresholds of CoTMPP-*x* gradually decrease with the increase of heat treatment temperature (the inset of Figure 3A), demonstrating that the valence states of Co element decrease accordingly.

Figure 3B shows the Fourier transform (FT) k^3-weight EXAFS curves of CoTMPP-*x* as well as the reference CoTMPP and Co foil. Clearly, the CoTMPP-400, 500 only displays a main peak at ca. 1.5 Å (without phase correction), corresponding to the first shell of Co-N scattering, and the Co-Co peak at ca. 2.2 Å is not detected. Differently, a Co-Co peak appears in CoTMPP-600, and its density gradually increases with the heat treatment temperature, accompanied by the gradual weakening of Co-N scattering from CoTMPP-400 to CoTMPP-800. Wavelet transform (WT) of Co K-edge EXAFS oscillations was performed to further explore the atomic dispersion of Co in the CoTMPP-*x* samples (Figures 3C, 3D, and S12). The WT contour plots of CoTMPP-400, 500 show only one intensity maximum at 1.5 Å, attributed to Co-N coordination, whereas CoTMPP-600 exhibits two clear intensity maxima at 1.5 and 2.2 Å, corresponding to Co-N and Co-Co coordination, respectively. In contrast, the WT contour plots of CoTMPP-700, 800 display only one main intensity maximum at 2.2 Å attributed to Co-Co coordination.
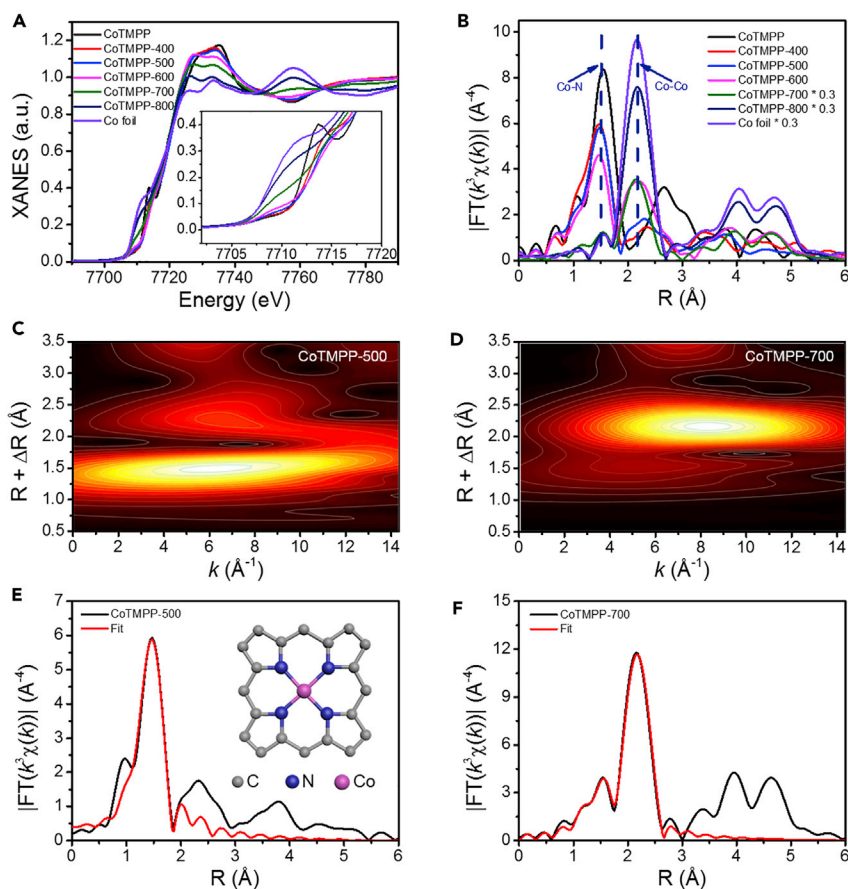
Figure 3. X-ray Absorption Fine Structure (XAFS) Measurements of the Catalysts

(A) XANES spectra at the Co K-edge of the CoTMPP-*x* catalysts, CoTMPP, and Co foil. The inset is the magnified image of pre-edge XANES spectra.

(B) Fourier transform (FT) at the Co K-edge of CoTMPP-*x* catalysts, CoTMPP, and Co foil.

(C and D) Wavelet transform (WT) of (C) CoTMPP-500 and (D) CoTMPP-700.

(E and F) The corresponding EXAFS R-space fitting curves for (E) CoTMPP-500 and (F) CoTMPP-700. Inset in (E) is the proposed model of Co-N_x center in CoTMPP-500.

Furthermore, to obtain the quantitative chemical configuration of Co atom in the CoTMPP-*x* samples, EXAFS fitting was carried out to extract the structure parameters. The structural models used for EXAFS fitting are presented in Figure S13. The EXAFS fitting parameters are listed in Table S2, and the fitting curves are shown in Figures 3E, 3F, and S14. For CoTMPP-500, there is only one coordination configuration (i.e., Co-N); the obtained coordination number of center atom Co is ca. 4, and the mean bond length of Co-N coordination is ca. 1.90 Å. By contrast, CoTMPP-700 possesses two coordination configurations, i.e., Co-N and Co-Co. In CoTMPP-700, the coordination number of center atom Co is ca. 3.8 and the mean bond length of Co-N coordination is ca. 1.91 Å, and the coordination number is ca. 3.4 and the mean bond length is 2.50 Å for the Co-Co coordination. The coordination numbers of Co-Co bond for CoTMPP-600, 700, 800 increase with the pyrolysis temperature, because higher pyrolysis temperature leads to bigger Co nanoparticles. According to the fitting results, the proposed local structure of CoTMPP-500 is constructed and presented in the inset of Figure 3E. Additional information of Co K-edge for CoTMPP-*x*, CoTMPP, and Co foil is provided in Figure S15. The XANES, EXAFS, and WT results strongly highlight that most of Co-N centers from CoTMPP molecule are kept in CoTMPP-400 and CoTMPP-500, whereas the Co-N centers are at least partially destroyed to form less active metallic Co nanoparticles in CoTMPP-600, 700, 800. These results are highly consistent with the above TGA, UV-Vis, EA, TEM, and aberration-corrected HAADF-STEM analyses.
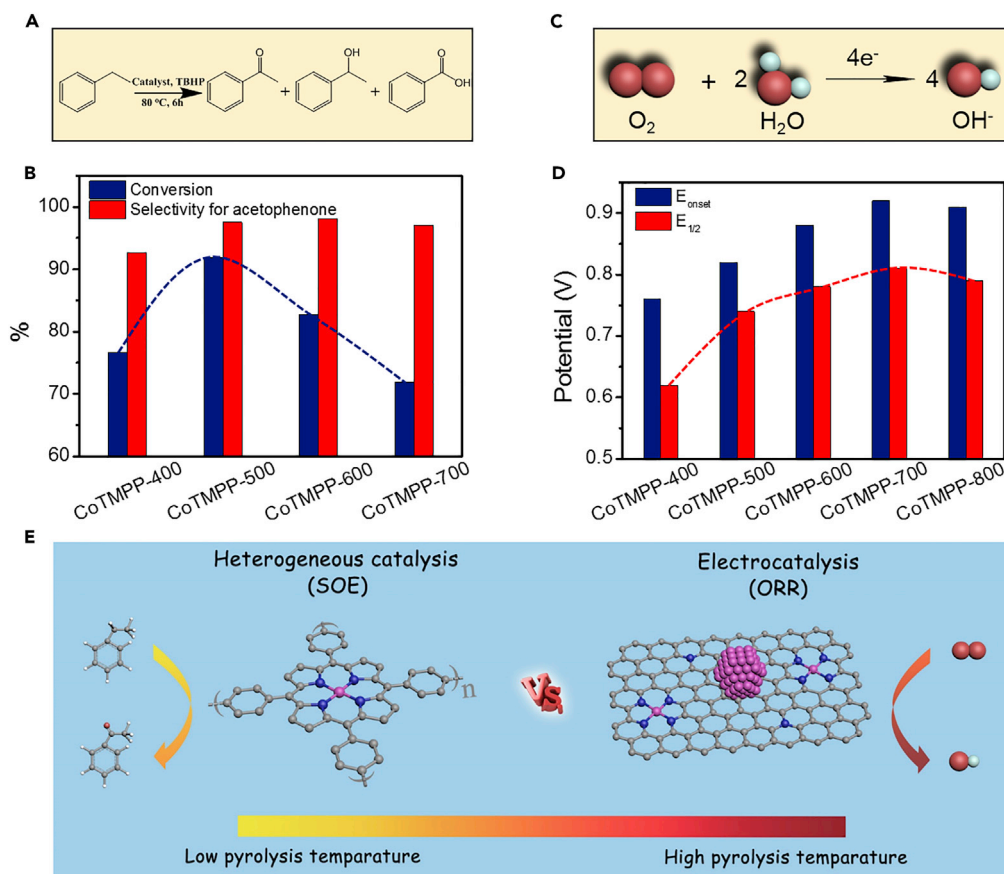
Figure 4. Heterogeneous Catalysis and Electrocatalysis Tests of the Catalysts

(A) Reaction equation of SOE.

(B) SOE catalytic performance of the CoTMPP-x catalysts.

(C) Schematic diagram of ORR in basic medium.

(D) ORR onset and half-wave potentials of the CoTMPP-x catalysts.

(E) Scheme of rational optimization of Co/N/C catalysts for heterogeneous catalysis (SOE) and electrocatalysis (ORR) processes.

Heterogeneous Catalysis and Electrocatalysis Tests

Selective oxidation of ethylbenzene (SOE) reaction and electrocatalytic ORR were chosen as typical heterogeneous catalysis and electrocatalysis reactions, respectively, to reveal the difference in optimizing the synthetic and structural parameters of the CoTMPP-x catalysts (Figure 4). First, we examined the CoTMPP-x and reference catalysts for SOE in aqueous phase with *tert*-butyl hydroperoxide (TBHP) as the oxidant, in which acetophenone is the main product with benzoic acid and 1-phenyl-ethylalcohol as the by-products (Figure 4A). The blank result confirms that the reaction activity is very low because of the ethylbenzene autoxidation (Figure S16) (Wang et al., 2014). When CoTMPP molecules supported on Ketjen black (CoTMPP/KJB) was used as the catalyst, a moderate activity with 40.3% conversion and 62.9% selectivity was displayed. In comparison, the CoTMPP-x catalysts prepared by the thermal treatment of CoTMPP show much better performance (Figure 4B). For example, CoTMPP-400 exhibits a conversion of 76.7% and a selectivity of 92.6%. Particularly, increasing the thermal treatment temperature to 500°C results in the optimal catalyst with 91.9% conversion and 97.5% selectivity. Further increasing the thermal treatment temperature, however, causes significant deterioration of the activity in the cases of CoTMPP-600 and CoTMPP-700.

The better catalytic performance of CoTMPP-400, 500 over CoTMPP/KJB demonstrates the superiority of polymer-like structure over the CoTMPP molecules for catalyzing SOE, probably because of the formation of a highly delocalized π-conjugated system that facilitates local electron transfer in the SOE process. The

inferior activity of CoTMPP-400 compared with CoTMPP-500 is attributed to the much lower porosity of CoTMPP-400, as a result of the absence of a robust mesoporous polymer-like structure. Although CoTMPP-600 and CoTMPP-700 possess higher specific surface areas than CoTMPP-500, the heat treatment at the temperature higher than 600°C generates less-active metallic Co nanoparticles by the decomposition of the highly active Co-N_4 centers and therefore results in worse catalytic activity. Besides, the reference catalyst prepared without SiO_2 template at 500°C (CoTMPP-500/SiO_2-free) exhibits a very poor catalysis activity, with only 19.5% conversion (nearly one-fifth of CoTMPP-500) and 63.0% selectivity (Figure S16), which further demonstrates the importance of porosity.

Interestingly, the stability tests indicate that the high thermal treatment temperature is beneficial to enhance the stability of the CoTMPP-*x* catalysts (Figure S17), probably because the graphitic carbon formed at high temperature can tolerate higher oxidation condition than the polymer-like materials obtained at low temperature. Moreover, the poisoning experiments of thiocyanate ions (SCN^-) on the SOE activity were carried out to further understand the nature of the active sites, as SCN^- is widely known to poison the metal-centered catalytic sites (Liang et al., 2015; Yang et al., 2016). The SCN^--poisoned CoTMPP-500 (CoTMPP-500/P) exhibits much lower SOE activity with a conversion of only 65.2% and a selectivity of 72.2% (Figure S18), clearly proving that the ionic cobalt species that coordinate with nitrogen are active sites in the CoTMPP-500 catalysts.

Electrocatalysis activities of CoTMPP-*x* and reference catalysts for ORR were studied using linear sweep voltammetry experiments in 0.1 M KOH solution (Figures 4C and S19). The CoTMPP/KJB catalyst shows a very poor ORR activity with an onset potential of 0.74 V and a half-wave potential of 0.61 V (Figure S20). As expected, thermal treatment of metal porphyrin can effectively enhance its ORR activity (Figure 4D). The ORR activity of CoTMPP-*x* catalysts increases with the thermal treatment temperature up to 700°C, at which the optimal catalyst (i.e., CoTMPP-700) is achieved with an onset potential of 0.92 V and a half-wave potential of 0.81 V. Further increase of thermal treatment temperature leads to slight decrease of the ORR activity. It is believed that an optimal balance of active site density, electron conductivity, and surface area is realized for CoTMPP-700 (Liang et al., 2013; Wu et al., 2011b). Metallic Co nanoparticles in CoTMPP-700 could be removed efficiently by an acid leaching step (Figure S21). Of note, we observed a considerably enhanced ORR activity, indicating that the Co-N centers are the main active sites in CoTMPP-700 (Figure S22). Similar to heterogeneously catalytic SOE, porosity is also proved to play a crucial role in electrocatalytic ORR by comparing the performance of CoTMPP-700 with the catalyst prepared without SiO_2 templates (CoTMPP-700/SiO_2-free, Figure S20).

DISCUSSION

The above heterogeneous catalysis in organic reactions and electrocatalysis results clearly reveal two key structural parameters for the Co/N/C catalyst system. First, the numbers of exposed single atom Co-N_x active sites greatly affect the catalytic performance for both heterogeneous catalysis and electrocatalysis processes. Second, the high electrical conductivity is imperative for electrocatalysts because of the needed rapid transport of electrons from the active sites within the catalyst to electrode during the electrocatalysis process, whereas the electrical conductivity is inessential for the heterogeneous catalysis in organic reactions due to the absence of long-range electron transport in heterogeneous catalysis (Figure 4E). Thereby, it is necessary to go to high-temperature thermal treatment (600–800°C) for preparing electrically conductive M/N/C electrocatalysts, albeit at the cost of the degradation of single-atom active Co-N_x active sites at high temperature (Figure 4E). For the preparation of M/N/C heterogeneous catalysts from molecular precursors for organic reactions, on the other hand, moderate thermal treatment temperature (400°C–500°C) would be optimal to form chemically and thermally stable polymer-like network that is composed of undecomposed and active single-atom Co-N_x centers (Figure 4E).

To summarize, we have demonstrated the nanoparticle templating preparation of a group of mesoporous Co/N/C catalysts from CoTMPP molecule precursor, ranging from polymer-like network with exclusive single-atom CoN_x sites to electrically conductive Co/N-doped carbons that consist of a mixture of Co nanoparticles and CoN_x sites, which were studied for both heterogeneous catalysis (in organic reactions) and electrocatalysis in a comparative perspective. Importantly, we found that the polymerized CoTMPP was highly efficient as a heterogeneous catalyst to heterogeneously catalyze the SOE, whereas the electrically conductive Co/N-doped carbon was superior for the electrocatalysis of oxygen reduction. Our results on the different synthetic and structural parameters in optimizing M/N/C materials for heterogeneous

catalysis and electrocatalysis will shed new light on the future development of earth-abundant catalysts for various reactions.

Limitations of Study

The polymerized cobalt porphyrin prepared at 500°C (i.e., CoTMPP-500) is highly active for catalyzing SOE, but not stable enough for recycling.

METHODS

All methods can be found in the accompanying Transparent Methods supplemental file.

SUPPLEMENTAL INFORMATION

Supplemental Information can be found online at https://doi.org/10.1016/j.isci.2019.04.032.

AUTHOR CONTRIBUTIONS

H.-W.L., Z.-Y.W., S.-H.Y. conceived and designed the experiments. M.-X.C. conducted the synthesis of the catalysts. Y.L. performed aberration-corrected HAADF-STEM and element mappings. S.-Q.C and J.Z. assisted with XAFS measurement and data analysis. Z.-Y.W. and M.-X.C performed the catalytic experiments. H.-W.L., Z.-Y.W., S.-H.Y., and M.-X.C. co-wrote the paper. All authors discussed the results and commented on the manuscript.

DECLARATION OF INTERESTS

The authors declare no competing interests.

REFERENCES

Banerjee, D., Jagadeesh, R.V., Junge, K., Pohl, M.M., Radnik, J., Brückner, A., and Beller, M. (2014). Convenient and mild epoxidation of alkenes using heterogeneous cobalt oxide catalysts. Angew. Chem. Int. Ed. 53, 4359–4363.

Bauer, I., and Knölker, H.-J. (2015). Iron catalysis in organic synthesis. Chem. Rev. 115, 3170–3387.

Bayatsarmadi, B., Zheng, Y., Vasileff, A., and Qiao, S.-Z. (2017). Recent advances in atomic metal doping of carbon-based nanomaterials for energy conversion. Small 13, 1700191.

Bezerra, C.W.B., Zhang, L., Lee, K., Liu, H., Marques, A.L.B., Marques, E.P., Wang, H., and Zhang, J. (2008). A review of Fe–N/C and Co–N/C catalysts for the oxygen reduction reaction. Electrochim. Acta 53, 4937–4951.

Chen, Z., Higgins, D., Yu, A., Zhang, L., and Zhang, J. (2011). A review on non-precious metal electrocatalysts for PEM fuel cells. Energy Environ. Sci. 4, 3167–3192.

Chung, H.T., Cullen, D.A., Higgins, D., Sneed, B.T., Holby, E.F., More, K.L., and Zelenay, P. (2017). Direct atomic-level insight into the active sites of a high-performance PGM-free ORR catalyst. Science 357, 479–484.

Cui, X., Li, Y., Bachmann, S., Scalone, M., Surkus, A.-E., Junge, K., Topf, C., and Beller, M. (2015). Synthesis and characterization of iron–nitrogen-

doped graphene/core–shell catalysts: efficient oxidative dehydrogenation of N-heterocycles. J. Am. Chem. Soc. 137, 10652–10658.

He, L., Weniger, F., Neumann, H., and Beller, M. (2016). Synthesis, characterization, and application of metal nanoparticles supported on nitrogen-doped carbon: catalysis beyond electrochemistry. Angew. Chem. Int. Ed. 55, 12582–12594.

Jagadeesh, R.V., Junge, H., Pohl, M.-M., Radnik, J., Brückner, A., and Beller, M. (2013a). Selective oxidation of alcohols to esters using heterogeneous Co_3O_4–N@C catalysts under mild conditions. J. Am. Chem. Soc. 135, 10776–10782.

Jagadeesh, R.V., Surkus, A.-E., Junge, H., Pohl, M.-M., Radnik, J., Rabeah, J., Huan, H., Schünemann, V., Brückner, A., and Beller, M. (2013b). Nanoscale Fe$_2$O$_3$-based catalysts for selective hydrogenation of nitroarenes to anilines. Science *342*, 1073–1076.

Jagadeesh, R.V., Murugesan, K., Alshammari, A.S., Neumann, H., Pohl, M.-M., Radnik, J., and Beller, M. (2017). MOF-derived cobalt nanoparticles catalyze a general synthesis of amines. Science *358*, 326–332.

Jaouen, F., Proietti, E., Lefevre, M., Chenitz, R., Dodelet, J.-P., Wu, G., Chung, H.T., Johnston, C.M., and Zelenay, P. (2011). Recent advances in non-precious metal catalysis for oxygen-reduction reaction in polymer electrolyte fuel cells. Energy Environ. Sci. *4*, 114–130.

Ji, Y., Li, Z., Wang, S., Xu, G., Li, D., and Yu, X. (2011). Durability of polytetraphenylporphyrin cobalt adsorbed on carbon black as an electrocatalyst for oxygen reduction. J. Electrochem. Soc. *158*, B139–B142.

Jiao, Y., Zheng, Y., Jaroniec, M., and Qiao, S.Z. (2015). Design of electrocatalysts for oxygen-and hydrogen-involving energy conversion reactions. Chem. Soc. Rev. *44*, 2060–2086.

Lefèvre, M., Proietti, E., Jaouen, F., and Dodelet, J.-P. (2009). Iron-based catalysts with improved oxygen reduction activity in polymer electrolyte fuel cells. Science *324*, 71–74.

Liang, H.-W., Wei, W., Wu, Z.-S., Feng, X., and Müllen, K. (2013). Mesoporous metal–nitrogen-doped carbon electrocatalysts for highly efficient oxygen reduction reaction. J. Am. Chem. Soc. *135*, 16002–16005.

Liang, H.-W., Brüller, S., Dong, R., Zhang, J., Feng, X., and Müllen, K. (2015). Molecular metal–N$_x$ centres in porous carbon for electrocatalytic hydrogen evolution. Nat. Commun. *6*, 7992.

Liu, W., Zhang, L., Yan, W., Liu, X., Yang, X., Miao, S., Wang, W., Wang, A., and Zhang, T. (2016a). Single-atom dispersed Co-N-C catalyst: structure identification and performance for hydrogenative coupling of nitroarenes. Chem. Sci. *7*, 5758–5764.

Liu, L., Concepción, P., and Corma, A. (2016b). Non-noble metal catalysts for hydrogenation: a facile method for preparing Co nanoparticles covered with thin layered carbon. J. Catal. *340*, 1–9.

Liu, W., Zhang, L., Liu, X., Liu, X., Yang, X., Miao, S., Wang, W., Wang, A., and Zhang, T. (2017). Discriminating catalytically active FeN$_x$ species of atomically dispersed Fe–N–C catalyst for selective oxidation of the C–H bond. J. Am. Chem. Soc. *139*, 10790–10798.

Liu, J., Zhu, D., Zheng, Y., Vasileff, A., and Qiao, S.-Z. (2018). Self-supported earth-abundant nanoarrays as efficient and robust electrocatalysts for energy-related reactions. ACS Catal. *8*, 6707–6732.

Lyons, T.W., and Sanford, M.S. (2010). Palladium-catalyzed ligand-directed C–H functionalization reactions. Chem. Rev. *110*, 1147–1169.

Marcilly, C. (2003). Present status and future trends in catalysis for refining and petrochemicals. J. Catal. *216*, 47–62.

Meng, C., Ling, T., Ma, T.Y., Wang, H., Hu, Z., Zhou, Y., Mao, J., Du, X.W., Jaroniec, M., and Qiao, S.Z. (2017). Atomically and electronically coupled Pt and CoO hybrid nanocatalysts for enhanced electrocatalytic performance. Adv. Mater. *29*, 1604607.

Neitzel, J.J. (2010). Enzyme catalysis: the serine proteases. Nat. Edu. *3*, 21.

Seh, Z.W., Kibsgaard, J., Dickens, C.F., Chorkendorff, I., Nørskov, J.K., and Jaramillo, T.F. (2017). Combining theory and experiment in electrocatalysis: insights into materials design. Science *355*, eaad4998.

Suzuki, T. (2011). Organic synthesis involving iridium-catalyzed oxidation. Chem. Rev. *111*, 1825–1845.

Wang, J., Liu, H., Gu, X., Wang, H., and Su, D.S. (2014). Synthesis of nitrogen-containing ordered mesoporous carbon as a metal-free catalyst for selective oxidation of ethylbenzene. Chem. Commun. *50*, 9182–9184.

Wang, J., Huang, Z., Liu, W., Chang, C., Tang, H., Li, Z., Chen, W., Jia, C., Yao, T., Wei, S., et al. (2017). Design of N-coordinated dual-metal sites: a stable and active Pt-free catalyst for acidic oxygen reduction reaction. J. Am. Chem. Soc. *139*, 17281–17284.

Wu, G., More, K.L., Johnston, C.M., and Zelenay, P. (2011a). High-performance electrocatalysts for oxygen reduction derived from polyaniline, iron, and cobalt. Science *332*, 443–447.

Wu, G., Johnston, C.M., Mack, N.H., Artyushkova, K., Ferrandon, M., Nelson, M., Lezama-Pacheco, J.S., Conradson, S.D., More, K.L., Myers, D.J., et al. (2011b). Synthesis-structure-performance correlation for polyaniline-Me-C non-precious metal cathode catalysts for oxygen reduction in fuel cells. J. Mater. Chem. *21*, 11392–11405.

Wu, Z.-Y., Xu, X.-X., Hu, B.-C., Liang, H.-W., Lin, Y., Chen, L.-F., and Yu, S.-H. (2015). Iron carbide nanoparticles encapsulated in mesoporous Fe-N-doped carbon nanofibers for efficient electrocatalysis. Angew. Chem. Int. Ed. *54*, 8179–8183.

Yang, S., Feng, X., Wang, X., and Müllen, K. (2011). Graphene-based carbon nitride nanosheets as efficient metal-free electrocatalysts for oxygen reduction reactions. Angew. Chem. Int. Ed. *50*, 5339–5343.

Yang, C., Fu, L., Zhu, R., and Liu, Z. (2016). Influence of cobalt species on the catalytic performance of Co-N-C/SiO$_2$ for ethylbenzene oxidation. Phys. Chem. Chem. Phys. *18*, 4635–4642.

Yin, P., Yao, T., Wu, Y., Zheng, L., Lin, Y., Liu, W., Ju, H., Zhu, J., Hong, X., Deng, Z., et al. (2016). Single cobalt atoms with precise N-coordination as superior oxygen reduction reaction catalysts. Angew. Chem. Int. Ed. *55*, 10800–10805.

Zhang, L., Wang, A., Wang, W., Huang, Y., Liu, X., Miao, S., Liu, J., and Zhang, T. (2015). Co–N–C catalyst for C–C coupling reactions: on the catalytic performance and active sites. ACS Catal. *5*, 6563–6572.

Zhou, P., Jiang, L., Wang, F., Deng, K., Lv, K., and Zhang, Z. (2017). High performance of a cobalt–nitrogen complex for the reduction and reductive coupling of nitro compounds into amines and their derivatives. Sci. Adv. *3*, e1601945.

Supplemental Information

Switching Co/N/C Catalysts

for Heterogeneous Catalysis and Electrocatalysis

by Controllable Pyrolysis of Cobalt Porphyrin

Zhen-Yu Wu, Ming-Xi Chen, Sheng-Qi Chu, Yue Lin, Hai-Wei Liang, Jing Zhang, and Shu-Hong Yu
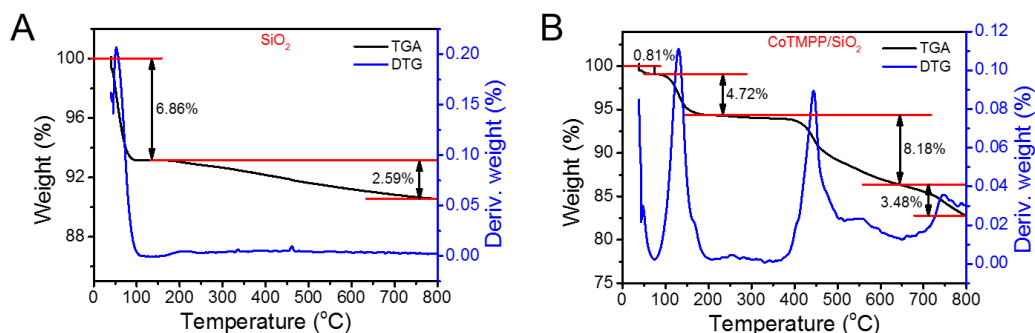
Supplemental Information

Switching Co/N/C Catalysts for Heterogeneous Catalysis and Electrocatalysis by Controllable Pyrolysis of Cobalt Porphyrin

Zhen-Yu Wu, Ming-Xi Chen, Sheng-Qi Chu, Yue Lin, Hai-Wei Liang,*
Jing Zhang, Shu-Hong Yu*

1. Supplemental Figures

Figure S1. TGA and DTG curves of SiO$_2$ templates and the CoTMPP/SiO$_2$ mixture under N$_2$ atmosphere, Related to Figure 2. (A) TGA and DTG curves of SiO$_2$ templates under N$_2$ atmosphere. (B) TGA and DTG curves of the CoTMPP/SiO$_2$ mixture under N$_2$ atmosphere. A degradation peaks at 227 ^{o}C in the DTG curve of CoTMPP is attributed to the loss of the physically absorbed water and residual small organic molecules for synthesizing CoTMPP (Figure 2A), while the intense degradation peak at 52 ^{o}C in the DTG curve of SiO$_2$ results from the loss of the physically absorbed water and many surface functional groups of SiO$_2$ (Figure S1A). After mixing CoTMPP and SiO$_2$ together, two clear degradation peaks at 48 ^{o}C and 130 ^{o}C are observed (Figure S1B), owing to the weight loss of CoTMPP and SiO$_2$. Besides, the degradation peaks at 444, 745 ^{o}C in the DTG curve of CoTMPP/SiO$_2$ well agree with the degradation peaks 442, 746 ^{o}C of CoTMPP. Therefore, the differential thermogravimetry (DTG) curve of CoTMPP/SiO$_2$ mixture matches well with those of CoTMPP and SiO$_2$. These results clearly indicated similar thermal decomposition process for pure CoTMPP and CoTMPP/SiO$_2$ mixture.
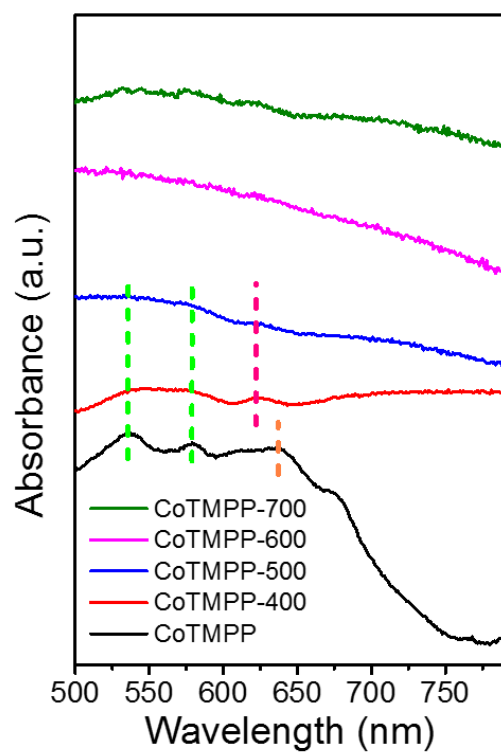
Figure S2. Solid UV-Vis spectra of CoTMPP molecule and the CoTMPP-*x* catalysts, Related to Figure 2.
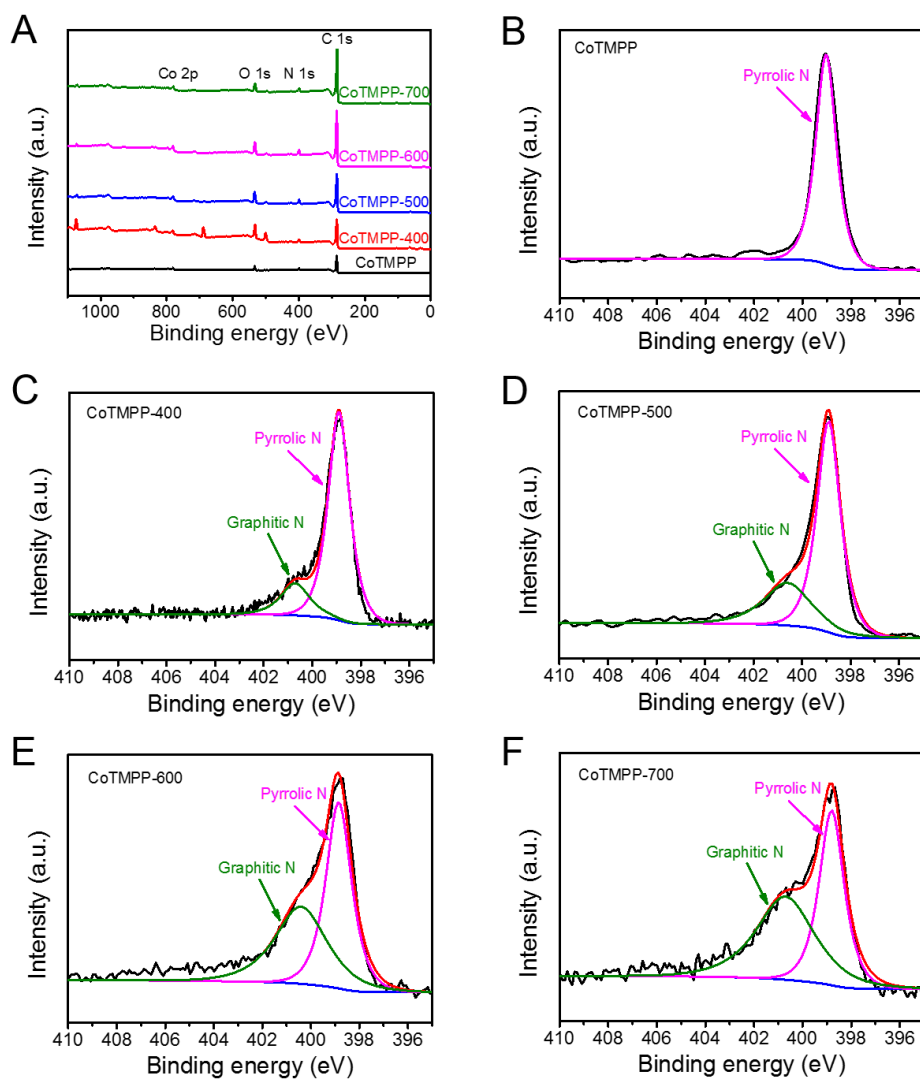
Figure S3. XPS results, Related to Figure 2. (A) XPS survey spectra of CoTMPP molecule and the CoTMPP-*x* catalysts. (B-F) High-resolution N 1s spectra of the CoTMPP molecule and the CoTMPP-400, 500, 600, 700 catalysts, respectively.
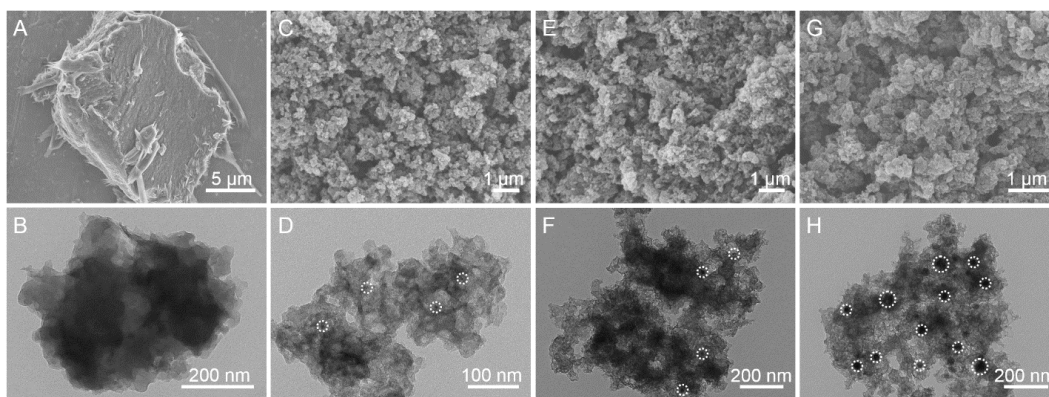
Figure S4. SEM and TEM images of CoTMPP-400, CoTMPP-600, CoTMPP-700, and CoTMPP-800, Related to Figure 2. (A, B) SEM and TEM images of CoTMPP-400. (C, D) SEM and TEM images of CoTMPP-600. (E, F) SEM and TEM images of CoTMPP-700. (G, H) SEM and TEM images of CoTMPP-800. The white circles in D, F, and H indicate the nanoparticles.
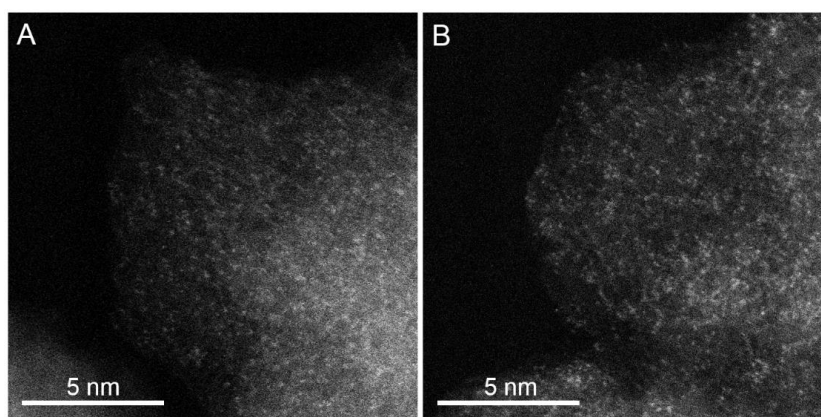
Figure S5. Two representative aberration-corrected HAADF-STEM images of the CoTMPP-500 catalyst at different areas, Related to Figure 2.
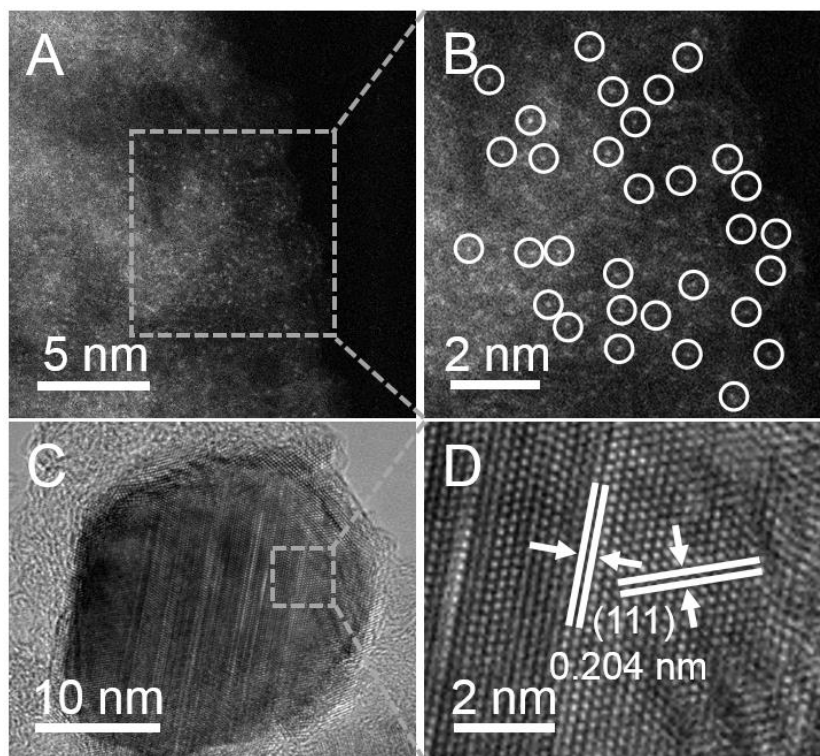
Figure S6. Aberration-corrected HAADF-STEM images and HRTEM images of CoTMPP-700, Related to Figure 2. (A, B) Aberration-corrected HAADF-STEM image and enlarged image of the CoTMPP-700 catalyst, showing the atomic distribution of Co elements in the carbon matrix. (C, D) high resolution TEM (HRTEM) images of a Co nanoparticle in CoTMPP-700. A set of lattice fringes with an interplanar distance of 0.204 nm is corresponding to the (111) plane of metallic Co.
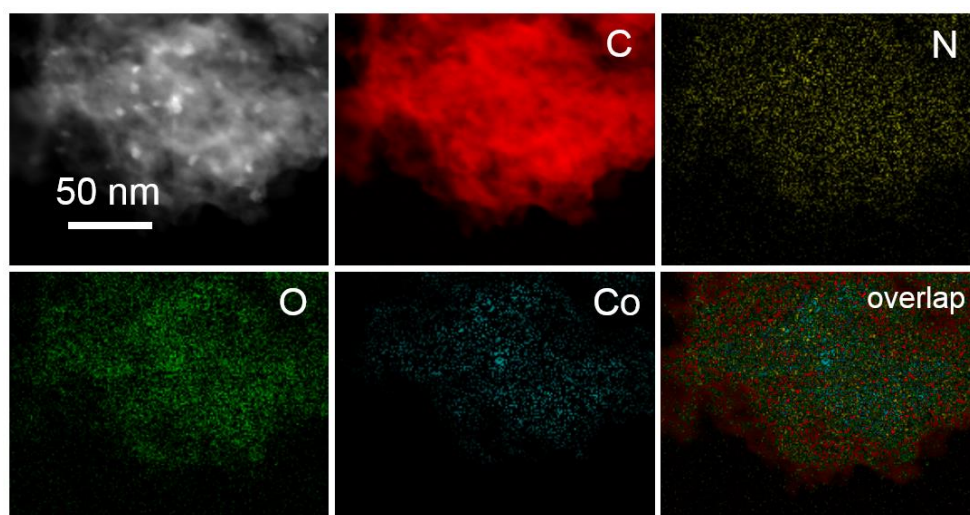

Figure S7. EELS elemental mapping images of the CoTMPP-700 catalyst, Related to Figure 2.
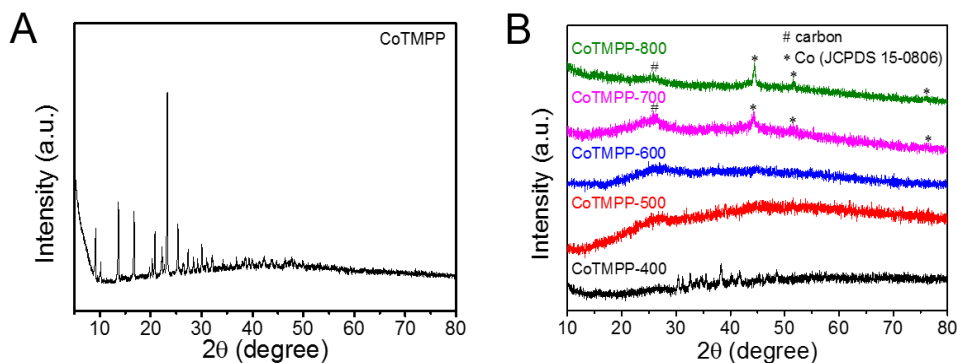
Figure S8. The XRD patterns of CoTMPP molecule and the prepared CoTMPP-*x* catalysts, Related to Figure 2. (A) The XRD pattern of CoTMPP molecule. (B) The XRD patterns of the prepared CoTMPP-*x* catalysts. At heat treatment temperature of 400 °C, the crystal structure of CoTMPP molecules has been destroyed, as proved by the change of the XRD diffraction peaks. No XRD peaks of Co nanoparticles are observed in CoTMPP-500, which is well consistent with its TEM, aberration-corrected HAADF-STEM, and elemental mapping results. The absence of characteristic peaks of Co nanoparticles in CoTMPP-600 is attributed to their ultrasmall size, as confirmed by the TEM image (Figure S4D). In contrast, three distinct diffraction peaks at 44.3, 51.5 and 76.1° are observed for CoTMPP-700 and CoTMPP-800, attributing to the diffractions of the (111), (200) and (220) faces, respectively, of metallic Co (JCPDS 15-0806). A broad peak near 26° can be attributed to the (002) plane of graphitic carbon.
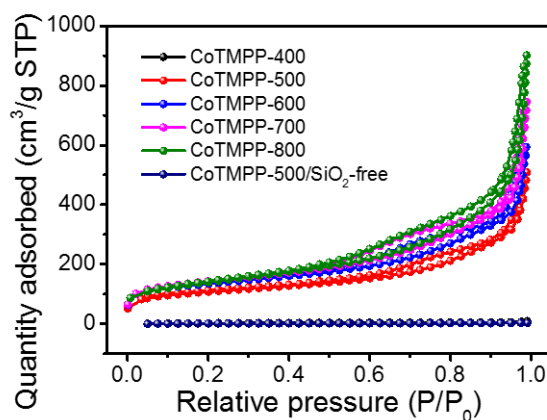

Figure S9. Nitrogen adsorption/desorption isotherms of the CoTMPP-*x* catalysts and the CoTMPP-500/SiO₂-free sample, Related to Figure 2.
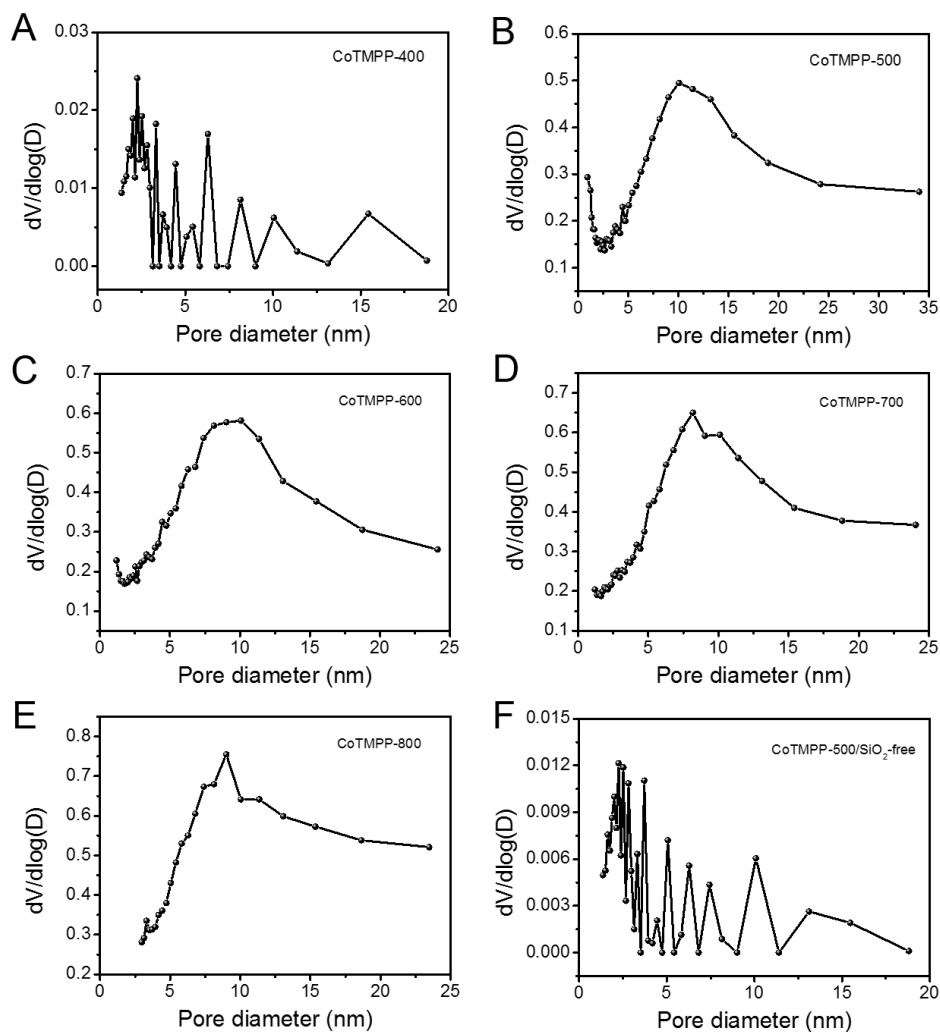
Figure S10. Textural properties, Related to Figure 2. (A-F) The pore size distribution curves of the CoTMPP-400, 500, 600, 700, 800 catalysts and the CoTMPP-500/SiO₂-free sample, respectively.
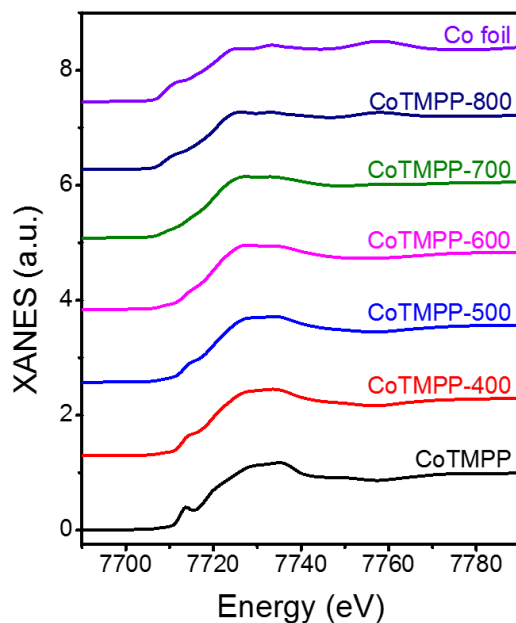
Figure S11. XANES spectra, Related to Figure 3. XANES spectra at the Co K-edge of the CoTMPP-*x* catalysts, CoTMPP, and Co foil.
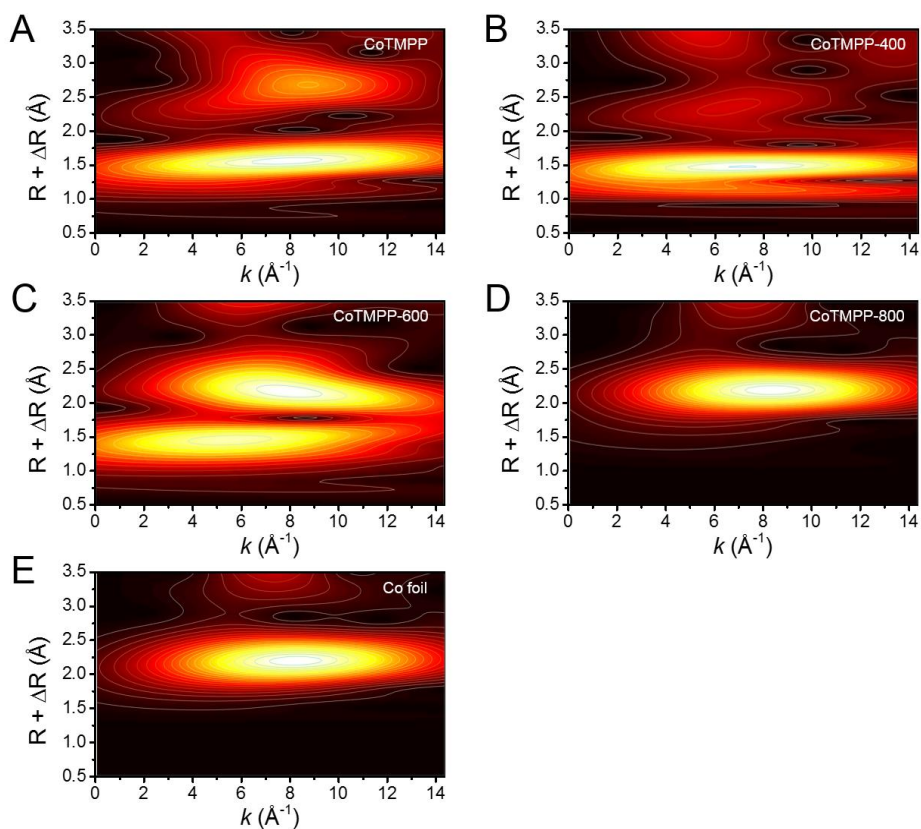

Figure S12. WT k^3-weighted χ(k)-function of the Co-K edge EXAFS spectra, Related to Figure 3. WT k^3-weighted χ(k)-function of the Co-K edge EXAFS spectra for (A) CoTMPP, (B) CoTMPP-400, (C) CoTMPP-600, (D) CoTMPP-800, and (E) Co foil.
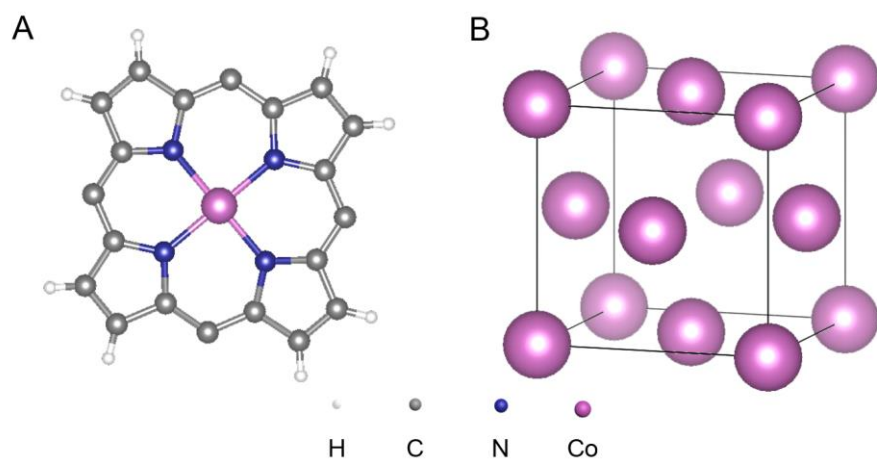
Figure S13. The structural models for fitting, Related to Figure 3. (A, B) The structural models used for EXAFS fitting.
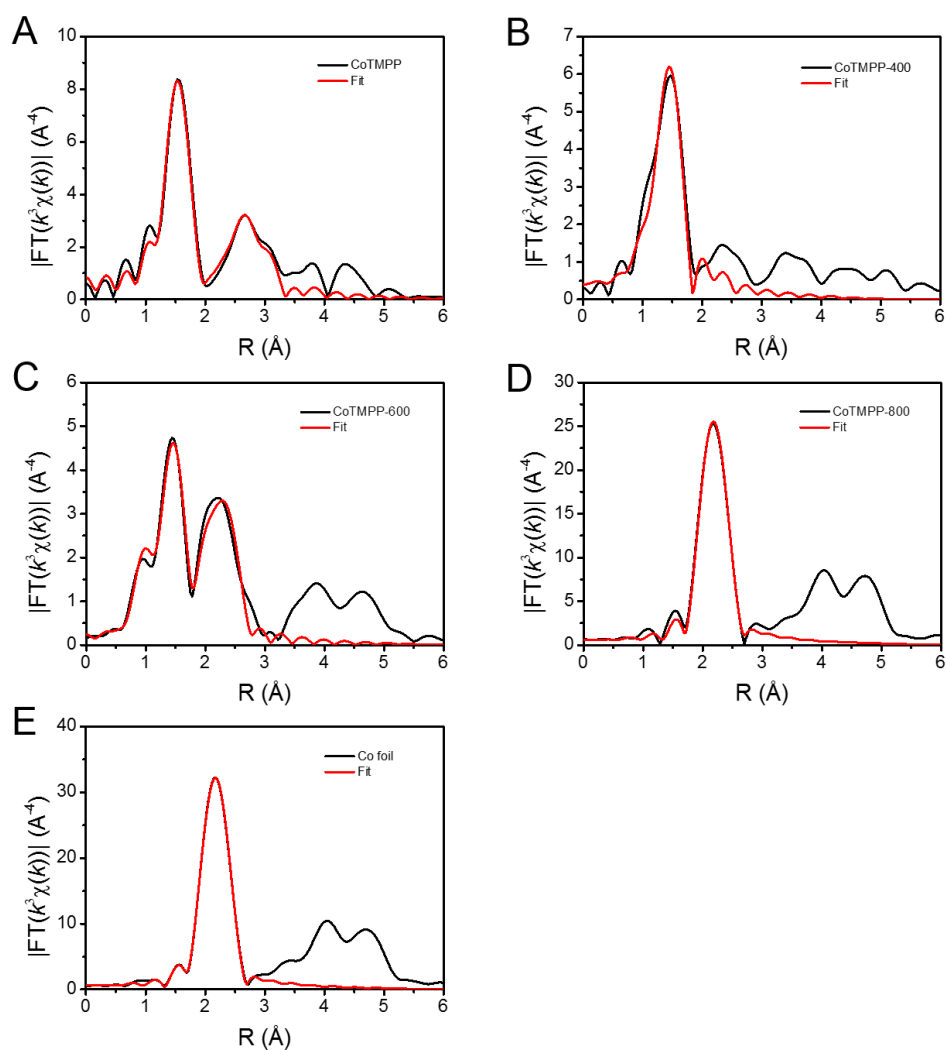

Figure S14. The corresponding EXAFS R-space fitting curves, Related to Figure 3. The corresponding EXAFS R-space fitting curves for (A) CoTMPP, (B) CoTMPP-400, (C) CoTMPP-600, (D) CoTMPP-800, and (E) Co foil.
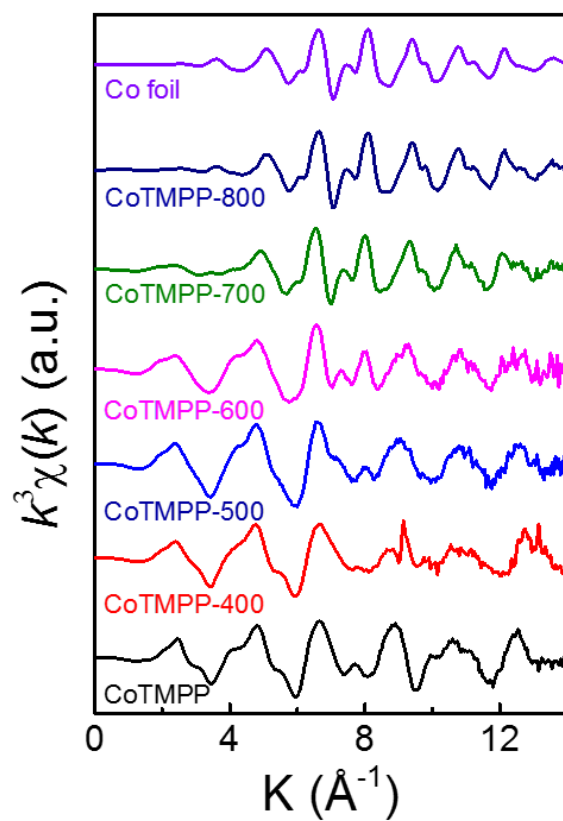
Figure S15. EXAFS in *k*-space for CoTMPP-*x* catalysts, CoTMPP and Co foil, Related to Figure 3.
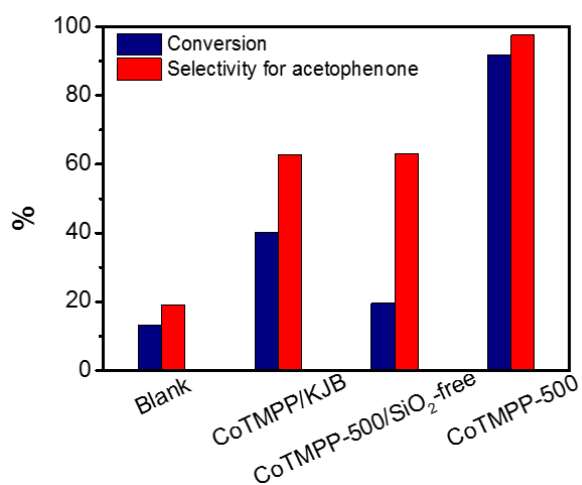

Figure S16. SOE catalytic performance of CoTMPP-500 and reference catalysts, Related to Figure 4.
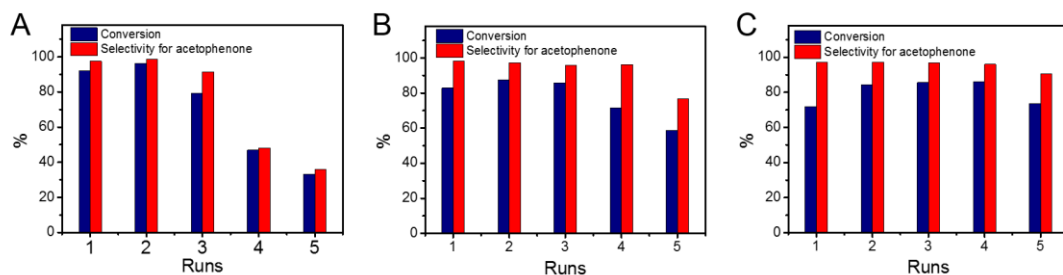
Figure S17. The stability tests of SOE, Related to Figure 4. The stability tests of (A-C) the CoTMPP-500, 600, 700 catalysts for SOE.
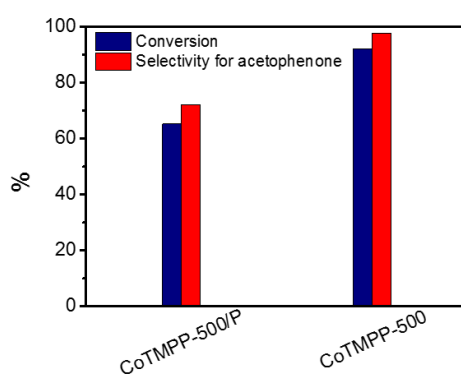

Figure S18. The poisoning experiments, Related to Figure 4. SOE catalytic performance of SCN$^-$-poisoned CoTMPP-500 (CoTMPP-500/P) and CoTMPP-500 catalysts.
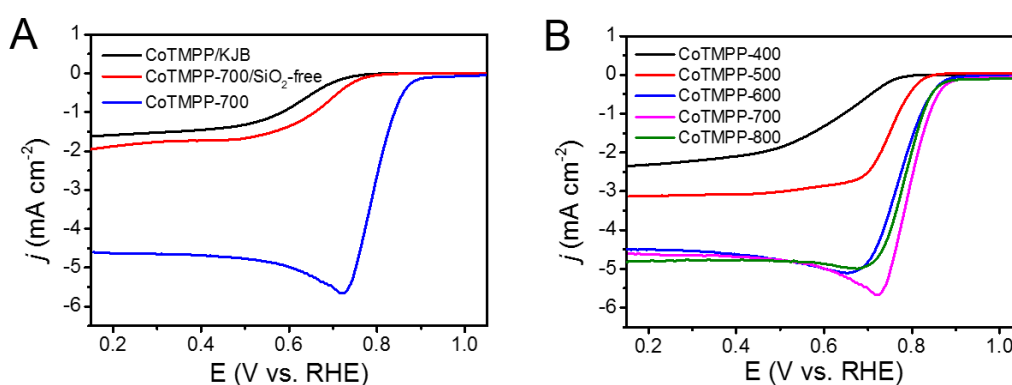
Figure S19. ORR performance, Related to Figure 4. (A) LSV curves of CoTMPP-700 and reference catalysts in 0.1 M KOH solution. (B) LSV curves of the CoTMPP-x catalysts in 0.1 M KOH solution.
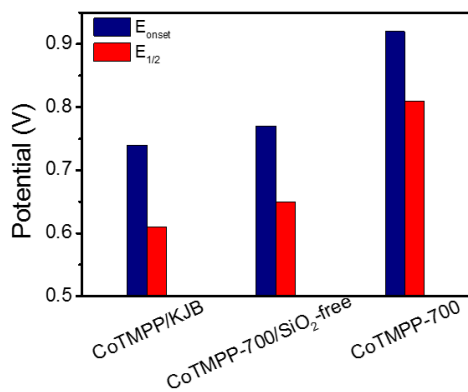
Figure S20. ORR onset and half-wave potentials of CoTMPP-700 and reference catalysts, Related to Figure 4.
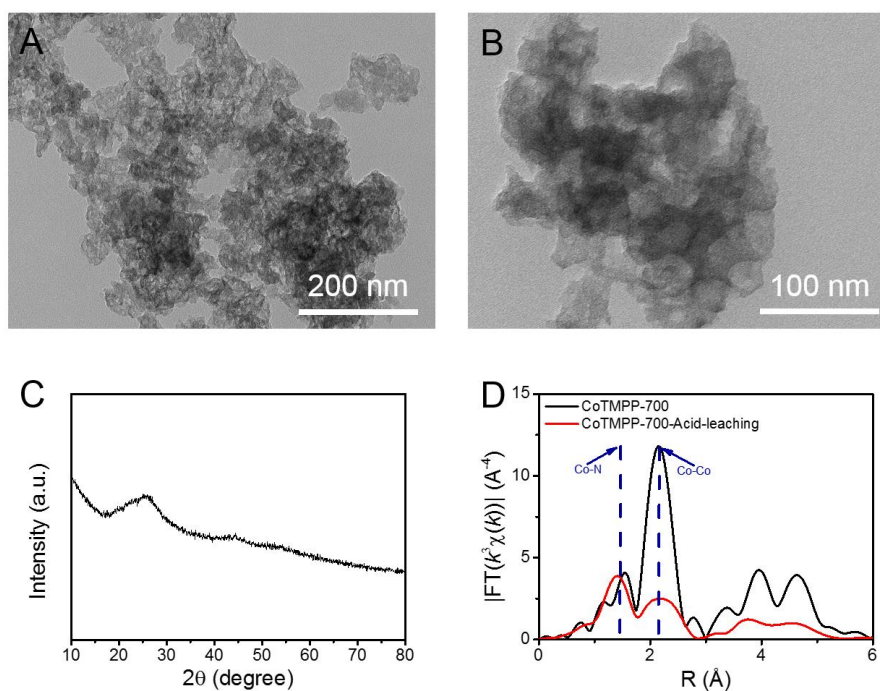
Figure S21. Characterization of the CoTMPP-700-Acid-leaching catalyst, Related to Figure 4. (A, B) The SEM images, (C) XRD pattern and (D) FT at the Co K-edge of CoTMPP-700-Acid-leaching.

Figure S22. ORR performance of CoTMPP-700 and CoTMPP-700-Acid-leaching, Related to Figure 4. (A) LSV curves of CoTMPP-700 and CoTMPP-700-Acid-leaching catalysts.

2. Supplemental Tables

Table S1. Chemical compositions of CoTMPP-*x* and CoTMPP by XPS tests, Related to Figure 2.

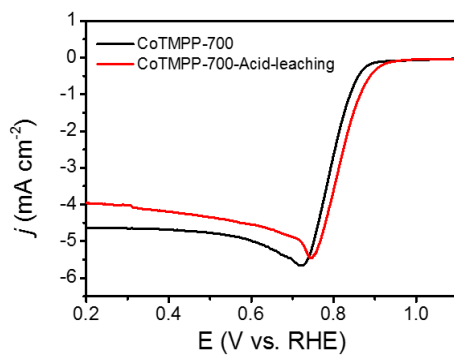| Samples	C (at%)	N (at%)	O (at%)	Co (at%)
CoTMPP	84.73%	6.1%	7.74%	1.43%
CoTMPP-400	75.94%	5.55%	16.86%	1.65%
CoTMPP-500	81.15%	6.23%	11.26%	1.36%
CoTMPP-600	83.85%	6.1%	8.96%	1.09%
CoTMPP-700	86.91%	4.69%	7.45%	0.95%

Table S2. Structural parameters of CoTMPP-*x* catalysts, CoTMPP and Co foil extracted from the EXAFS fitting, Related to Figure 3. (S_0^2=0.90)

Sample	Shell	N	R (Å)	σ^2 ($10^{-3}Å^2$)	ΔE_0 (eV)	R factor
CoTMPP	Co-N 1st shell	4(fixed)	1.939±0.009	3±0.6	8.06±1.32	0.012
	Co-C 2nd shell	8(fixed)	2.968±0.013	5.5±1.8		
	Co-C 3rd shell	2.7±1.5	3.318±0.021	10±5.3		
CoTMPP -400	Co-N	4.7±1.1	1.893±0.024	6.7±3.2	0.0±3.6	0.012
CoTMPP -500	Co-N	4.0±0.7	1.897±0.016	5.9±2.1	1.20±2.40	0.005
CoTMPP -600	Co-N	5.0±1.9	1.905±0.024	11.5±4	-0.35±3.91	0.010
	Co-Co	1.6±0.5	2.543±0.023	8.2±3	11.28±3.23	
CoTMPP -700	Co-N	3.8±1.0	1.906±0.03	12±4.1	-1.75±4.03	0.005
	Co-Co	3.4±0.3	2.502±0.007	5.7±0.8	3.73±1.19	
CoTMPP -800	Co-Co	6.8±0.7	2.497±0.006	5.3±0.8	-0.007±0.006	0.01
Co foil	Co-Co	12(fixed)	2.494±0.002	6.5±0.3	6.76±0.35	0.001

S_0^2 is the amplitude reduction factor; N is the coordination number; R is interatomic distance (the bond length between central atoms and surrounding coordination atoms); σ^2 is Debye-Waller factor (a measure of thermal and static disorder in absorber-scatterer distances); ΔE_0 is edge-energy shift (the difference between the zero kinetic energy value of the sample and that of the theoretical model). R factor is

used to value the goodness of the fitting. This values were fixed during EXAFS fitting, based on the known structure of CoTMPP and Co foil.

Transparent Methods

Chemicals.
CoTMPP, SiO_2 and Ketjen black were purchased from Tokyo chemical industry Co., Ltd, Sigma-Aldrich, and AkzoNobel, respectively. Other chemicals were commercially available from Sinopharm Chemical Reagent Co. Ltd (China) and used as received without further purification.

Synthesis of Co/N/C catalysts.
In a typical synthesis, 200 mg CoTMPP and 200 mg fumed SiO_2 (7 nm) were added into 120 mL N, N-dimethyl formamide (DMF) under 50 °C. After vigorous stirring for 1 h, the solvent was removed by using a rotary evaporator. Then the mixed powder was placed on a crucible in a quartz tube furnace and thermally treated at a range of temperature from 400 °C to 800 °C for 2 h with a ramp rate of 5 °C min^{-1} under N_2 flow. The as-obtained powder was subsequently etched by 2.0 mol L^{-1} NaOH for 3 days to remove SiO_2 templates and then experienced a second pyrolysis under 5% H_2/Ar atmosphere at the same temperature to get the final catalyst, CoTMPP-x (x is the pyrolysis temperature). Several reference catalysts were also prepared for comparison. For the synthesis of Ketjen black supported CoTMPP catalyst (CoTMPP/KJB), the commercially available KJB was firstly activated by a mixed concentrated H_2SO_4/HNO_3 solution (the volume ration of concentrated H_2SO_4 and concentrated HNO_3 is 3:1) at 80 °C for 2 h. Then, the activated KJB was mixed with CoTMPP in DMF with a mass ratio of 4:1, and the solvent was removed by using a rotary evaporator to get CoTMPP/KJB catalyst. Template-free synthesized catalysts, CoTMPP-500/SiO_2-free and CoTMPP-700/SiO_2-free, were prepared by direct thermal treatment of pure CoTMPP twice at the corresponding temperatures under N_2 and 5% H_2/Ar flow, respectively. To obtain poisoned samples (CoTMPP-500/P), CoTMPP-500 was firstly immersed in 1 mol L^{-1} KSCN aqueous solution at 60 °C for 3 h and then dried to get the products.

Instrumentation.
SEM images were captured on a Zeiss Supra 40 scanning electron microscope at an acceleration voltage of 5 kV. TEM images were observed by using a Hitachi H7700 transmission electron microscope with a CCD imaging system and an accelerating voltage of 100 kV. XRD data was obtained on a Philips X'Pert PRO SUPER X-ray diffractometer equipped with graphite monochromatic Cu Kα radiation (λ = 1.54056 Å). XPS was carried out on an X-ray photoelectron spectrometer (ESCALab MKII) with an excitation source of Mg Kα radiation (1253.6 eV). Solid UV-Vis absorption spectra were recorded on a Shimadzu UV-2550 spectrophotometer (Kyoto, Japan). TGA was tested by a TGA Q5000IR analyzer under N_2 flow with a temperature ramp

of 10 °C min^{-1}. HAADF-STEM, element mappings, and high-resolution TEM (HRTEM) were acquired using a JEM-ARM 200F Atomic Resolution Analytical Microscope operating at an accelerating voltage of 200 kV. Elemental mappings were collected using a Gatan GIF Quantum 965 instrument. N_2 sorption analysis was performed using an ASAP 2020 accelerated surface area and porosimetry instrument (Micromeritics), equipped with automated surface area, at 77 K using Barrett-Emmett-Teller (BET) calculations for the surface area. The pore size distribution plot was analyzed from the adsorption branch of the isotherm based on the Barrett-Joyner-Halenda (BJH).

XAFS measurement and data analysis.
XAFS spectra at the Co K-edge (7709 eV) were measured at the beamline 1W1B station of the Beijing Synchrotron Radiation Facility (BSRF), China. The Co K-edge XANES data were recorded in a fluorescence mode. Co foil and CoTMPP were used as the references. The storage ring was working at the energy of 2.5 GeV with an average electron current of 250 mA. The hard X-ray was monochromatized with Si(111) double-crystals. The acquired EXAFS data were extracted and processed according to the standard procedures using the ATHENA module implemented in the IFEFFIT software packages. The k^3-weighted EXAFS spectra were obtained by subtracting the post-edge background from the overall absorption and then normalizing with respect to the edge-jump step. Subsequently, k^3-weighted $\chi(k)$ data in the k-space ranging from 2.5-11.2 Å^{-1} were Fourier transformed to real (R) space using a hanning windows (d$_K$ = 1.0 Å^{-1}) to separate the EXAFS contributions from different coordination shells.

Selectively catalytic oxidation of ethylbenzene.
Typically, 5 mg catalyst, ethylbenzene (0.5 mmol), H_2O (1 mL), and TBHP (70% solution in water, 500 µL) were added into a 15 mL quartz glass tube. The reaction vessel was heated at 80 °C for 6 h with magnetic stirring at 1500 rpm. Afterwards, 77 µL anisole was added into the reaction system and used as internal standard. 10 mL ethyl acetate was used to extract the organic compounds in the reaction system. Finally, the reaction products were determined by using a Shimadzu gas chromatograph with an FID detector (GC-FID) and high purity nitrogen as the carrier gas. As for CoTMPP/KJB catalyst, 25 mg material was used for catalytic oxidation of ethylbenzene measurement. For stability tests, the used catalyst was recovered by centrifugation under 9000 rpm for 12 min, thoroughly washed with ethanol and water, and dried under vacuum at 60 °C overnight. Then it was reused under similar conditions.

Electrocatalytic ORR measurements.
The electrochemical measurements were carried out using a three-electrode cell system on WaveDriver 20 bipotentiostat (Pine Instrument Company, USA) controlled at room temperature. Ag/AgCl (3.5 M KCl) and platinum foil were used as the reference electrode and the counter electrode, respectively. A glassy carbon (GC) disk

whose diameter is 5 mm (disk geometric area is 0.196 cm^2) served as the substrate for the working electrode. To prepare the working electrode for electrochemical measurements, 10 mg catalyst (25 mg for CoTMPP/KJB catalyst) was blended with 100 μL Nafion solution (0.5 wt%) and 920 μL and ultrasonicated to form a homogenous catalyst ink. The working electrode was prepared by pipetting 12 μL of the ink onto GC electrode and drying at room temperature, leading to a catalyst loading of ca. 0.6 mg cm^{-2}. Before measurements, the electrolyte was saturated with N_2/O_2 by bubbling N_2/O_2 prior to the start of each experiment for 30 min. The ORR activities of catalysts were evaluated by rotating disk electrode (RDE) measurements in O_2-saturated 0.1 mol L^{-1} KOH aqueous solution at 1600 rpm with a negative scan rate of 5 mV s^{-1}. In order to remove the double layer capacitance, the voltammogram was evaluated in the electrolyte that was deaerated by purging it with N_2 before.